Letter | Editors' Suggestion

Enhanced spin Seebeck effect in the paramagnetic phase of the three-dimensional Heisenberg antiferromagnet $RbMnF_3$

J. D. M. de Lima, P. R. T. Ribeiro, F. L. A. Machado, and S. M. Rezende*
Departamento de Física, Universidade Federal de Pernambuco, 50670–901, Recife, Pernambuco, Brazil

(Received 1 February 2023; revised 19 March 2023; accepted 27 March 2023; published 11 April 2023)

$RbMnF_3$ is an insulating antiferromagnet with a perovskite crystal structure and Néel temperature $T_N = 83$ K. Having magnetic ions with a S electronic ground state in a cubic arrangement, its magnetic anisotropy vanishes so that it is a nearly perfect three-dimensional Heisenberg antiferromagnet. Here, we report measurements of the spin Seebeck effect (SSE) in bulk samples of $RbMnF_3$ with the shape of a slab onto which a thin Pt film strip is deposited. By applying a thermal gradient perpendicular to the slab plane, we detect an electric voltage along the Pt strip due to the charge current resulting from the conversion of the thermally generated spin current by means of the inverse spin Hall effect. By varying the magnetic field applied on the plane of the slab, we observe the antisymmetric step variation typical of the SSE both in the spin-flop and paramagnetic phases. Surprisingly the SSE increases with temperature in the paramagnetic phase and becomes comparable to the one in the ordered phase. This enhancement is attributed to a combination of the free spin fluctuations of paramagnetic insulators with the thermal conduction of long-lived paramagnons made possible by the short-range order that persists above T_N.

DOI: 10.1103/PhysRevB.107.L140406

The discovery of the spin Seebeck effect (SSE) in 2008 by Uchida *et al.* [1] gave birth to a new area of spintronics, called spin caloritronics. Since then, the new area has attracted considerable attention for its scientific interest and potential applications in thermomagnetic devices [2–9]. The spin Seebeck effect, a magnetic analog of the ancient thermoelectric Seebeck effect, consists of the generation of a spin current by a thermal gradient in a magnetic material. The initial experiments on the SSE were performed with a thermal gradient applied along a magnetic film both with the metallic ferromagnet permalloy [1] and the ferrimagnetic insulator yttrium iron garnet (YIG) [10] in the so-called transverse configuration. The effect was detected by electric voltage signals measured along thin Pt strips deposited on the magnetic film due to the conversion of the spin current into charge current by means of the inverse spin Hall effect (ISHE) [11–15].

Soon after the first experiments, Uchida *et al.* reported the observation of the SSE with the thermal gradient applied perpendicularly to the plane of a YIG film in contact with a thin Pt layer [16]. This generates a spin current in the same direction of the thermal gradient, and, for this reason, the phenomenon was called longitudinal spin Seebeck effect (LSSE). In this case, the spin current flows into the Pt layer where it is converted into a charge current by the ISHE and detected by the associated voltage [2,16]. The LSSE proved to be much more robust than the effect in the transverse mode so that the longitudinal configuration has become the standard method for studying the spin Seebeck effect [2–9].

After the initial studies of the SSE in ferro- and ferrimagnetic materials, the investigation of this effect turned to antiferromagnetic (AF) insulators and several new interesting phenomena were revealed [17–23]. This class of magnetic materials has been gaining renewed attention due to the emergence of the subfield of AF spintronics [24–33]. Commonly employed passively to pin the magnetization of an adjacent ferromagnetic layer in spin-valve devices through the interfacial exchange bias [34–36], AF materials have very unique dynamic features that might have applications in novel devices.

In this Letter, we report experimental measurements of the SSE in the three-dimensional (3D) antiferromagnet $RbMnF_3$. As in the well-studied uniaxial antiferromagnet MnF_2, the ground state of the magnetic Mn^{2+} ions in $RbMnF_3$ has configuration $3d^5(^6S_{5/2})$ with no single-ion angular momentum. In MnF_2, the tetragonal arrangement of the magnetic ions results in a sizeable anisotropy due to the dipolar interaction, $H_A \approx 10$ kOe [37,38]. However, $RbMnF_3$ has a perovskite crystal structure as shown in Fig. 1(a) with no measurable distortion from cubic symmetry [39] so that the dipolar anisotropy vanishes. As a result, $RbMnF_3$ has very small magnetic anisotropy, $H_A \approx 4.5$ Oe, and is considered a prototype 3D Heisenberg antiferromagnet [39–47]. We have measured the SSE in two samples of $RbMnF_3$ with the applied field varying in the range $-80 < H < 80$ kOe and at temperatures from 5 to 300 K. At temperatures below the Néel temperature $T_N = 83$ K, the magnetic system is in an AF-ordered state, and at higher temperatures, it is the paramagnetic phase. Due to the very small anisotropy, the field for the transition from the antiferromagnetic to the spin-flop configuration is only $H_{SF} = 2.4$ kOe [40,41]. Thus, in the field range of our experiments, we basically measure the SSE in the spin-flop and in the paramagnetic phases.

*Corresponding author: sergio.rezende@ufpe.br

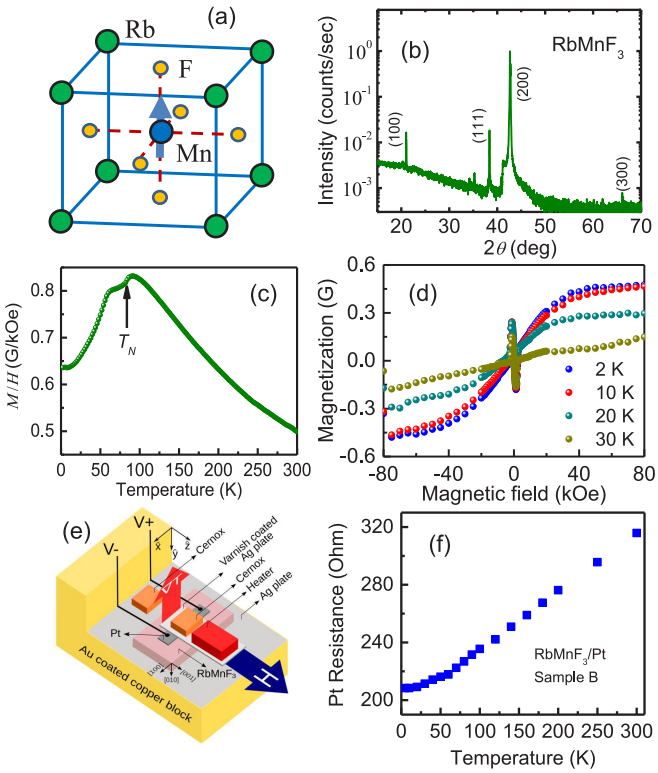

FIG. 1. (a) Crystal structure of $RbMnF_3$. (b) X-ray diffraction pattern of the $RbMnF_3$ bulk sample used to fabricate the devices for measuring the SSE. (c) Temperature variation of the magnetization of $RbMnF_3$ measured in a static field $H = 1.0$ kOe applied in the [100] direction. (d) Magnetization vs field measured at the temperatures indicated. (e) Sketch of the sample mount showing the heater and thermometer arrangements. (f) Temperature variation of the resistance of the Pt strip measured in device B.

The experiments were carried out with two samples of $RbMnF_3$ in the shape of slabs with thickness about 1 mm obtained by cleaving a bulk rectangular prism of dimensions $3 \times 4 \times 7\,\text{mm}^3$ with all faces on $\langle 100 \rangle$ planes, cut from a single crystal boule grown by the Czochralski method. Two devices were made by sputter depositing Pt strips of thickness 10 nm and width 1.2 mm on the cleaved surface along the larger dimension of the slab. Sample B (of blue) had length 7.1 mm, width 3.0 mm, and thickness 1.0 mm, whereas sample *R* (of red) had length 4.5 mm, width 3.0 mm, and thickness 1.0 mm both with edges along $\langle 100 \rangle$ crystal directions. Two characterization measurements were performed in the bulk sample before slicing the slabs, x-ray diffraction and magnetization. Figure 1(b) shows the x-ray diffraction pattern of the sample measured with a Rigaku x-ray diffractometer, model Smartlab, with the Cu $K\alpha$ radiation ($\lambda = 1.5418$ Å), exhibiting the strong peak corresponding to the (200) plane of $RbMnF_3$ and the smaller peaks of the (100), (111), and (300) planes. Figure 1(c) shows the temperature variation of the magnetization M measured in the bulk sample before slicing, whereas Fig. 1(d) shows magnetization vs field measured at various temperatures. The measurements were performed with the AC/DC Magnetometry System modulus of a Quantum Design Physical Property Measurement System (PPMS) with a field $H = 1$ kOe applied along the [001] axis. The Néel temperature $T_N = 83$ K corresponds to the peak in dM/dT shown in Fig. 1(c). In Fig. 1(d), the rapid variation near the origin is due to the spin-flop transition.

Figure 1(e) shows a sketch of the sample mount used to apply the temperature gradient and to measure the voltages in the Pt strip. A strain gauge ($R = 348.6\,\Omega$) soldered on a silver plate was used to heat the side of the metallic layer, whereas the bottom side of the $RbMnF_3$ slab was glued to a gold coated copper block by means of a thin layer of diluted GE varnish. Two Cernox thermometers (model CX-1050-SD-HT) were used to measure the temperatures on the two sides of the sample, one attached close to the heater and one attached to the gold-coated copper block.

Copper leads attached to the puck with silver paint and an external DC power supply were used to heat the silver plate for setting the temperature difference ΔT_{set} between the silver plate and the copper block, which is measured by the two thermometers. The PPMS was operated in the user bridge mode with the temperature stabilized to within ± 0.01 K and varied from 5 to 300 K.

The magnetic-field H, applied along the [001] crystal direction, transversely to the long dimension of the Pt strip, was swept from -80 to $+80$ kOe with varying steps: 2.5 kOe for $80\,\text{kOe} > |H_0| > 5\,\text{kOe}$ and 0.25 kOe for $|H_0| < 5\,\text{kOe}$, keeping the temperature fixed. The temperature difference across the sample structure was determined by measuring the temperature T_s at the silver plate (heater side) and T_{cb} at the copper block. As will be shown later, the temperature difference ΔT across the $RbMnF_3$ sample is smaller than the temperature difference measured by the two thermometers, $\Delta T_{\text{set}} = T_s - T_{cb}$ because the two layers of GE varnish used to glue the sample to the silver plate and to the copper block have thermal resistances that cannot be neglected, especially at low temperatures. Two thin copper wires attached to the ends of the Pt strip with silver paste were connected to the PPMS for measuring the voltage produced by the SSE-ISHE effects. Figure 1(f) shows the temperature variation of the Pt strip resistance R_{Pt} used to calculate the SSE current. From the measured voltage vs H data we subtracted a function symmetric in field about $H = 0$ in order to obtain the antisymmetric contribution $V_{\text{SSE}}(H) = -V_{\text{SSE}}(-H)$ produced by the spin Seebeck effect. The symmetric component is attributed to the planar Nernst effect [21,22,48] in the Pt film under the magnetic proximity effect due to the residual in-plane thermal gradient.

Figure 2 shows the magnetic-field dependence of the SSE current $I_{\text{SSE}} = V_{\text{SSE}}/R_{\text{Pt}}$ measured in the Pt strip of the two $RbMnF_3$/Pt samples at several temperatures under a set temperature difference ΔT_{set} as indicated in each plot. All data exhibit the steplike behavior characteristic of the SSE. This charge current is produced by the ISHE conversion of the spin current generated by the temperature gradient across the AF sample. The application of a temperature gradient ∇T across an AF insulator generates a spin current density given by $\vec{J}_S = -C_s \nabla T$, where C_s is a coefficient that depends on the mechanism and the material parameters, temperature, and applied field intensity. The spin current $\vec{J}_S$ flows into the Pt layer and is converted into a charge current by the ISHE with a current density given by $\vec{J}_C = \theta_{SH} \vec{J}_S \times \hat{\sigma}$, where θ_{SH} is the

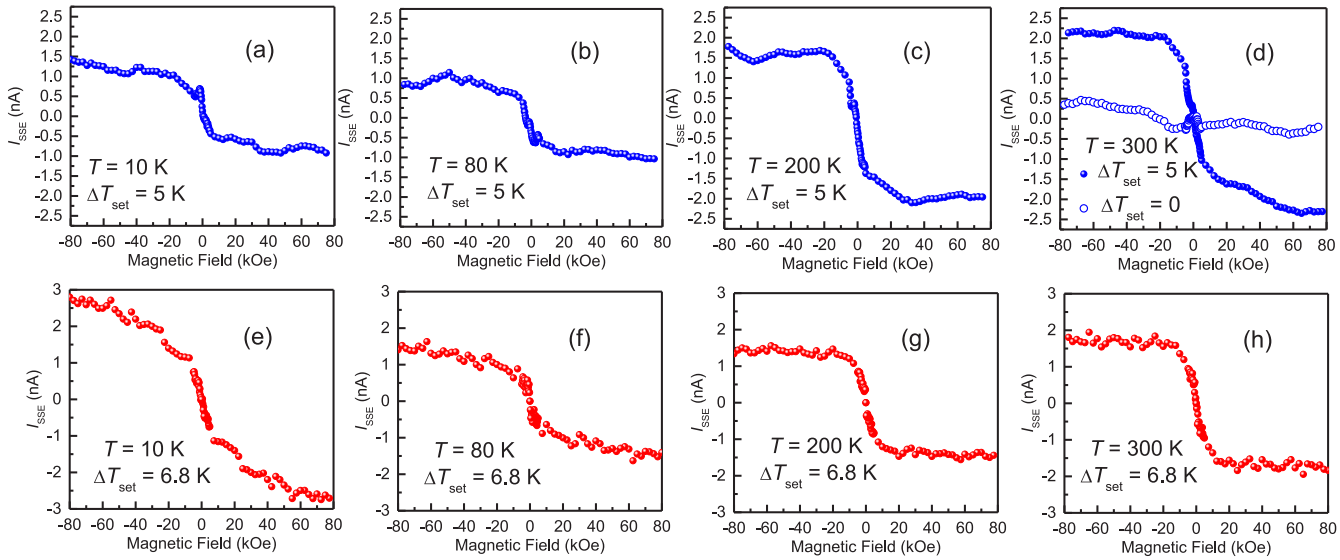

FIG. 2. Variation with magnetic-field H of the SSE current measured in the Pt strip of the two $RbMnF_3$/Pt samples at several values of the copper block temperature $T = T_{cb}$ as indicated. Plots (a)–(d) measured in sample B with set temperature difference $\Delta T_{set} = 5\,K$ and plots (e)–(h) measured in sample R with $\Delta T_{set} = 6.8\,K$.

spin Hall angle, and $\hat{\sigma}$ is the spin polarization. As the field is scanned and reverses direction at $H = 0$, the sign of $\hat{\sigma}$ in the Pt layer changes, and so does the sign of the voltage. The data in Fig. 2 show clearly that the measurements in the two samples are consistent with each other. A remarkable result is the fact that the SSE current at $T > T_N$ in the paramagnetic phase is comparable to the one in the ordered phase with the spin-flop configuration at $T < T_N$.

Figure 3(a) shows another typical signature of the SSE, the linear variation of the SSE voltage with the temperature difference ΔT_{set} applied to the $RbMnF_3$/Pt sample B structure. Interestingly, the data were obtained with the copper block maintained at room temperature $T = 300\,K$ at which the AF material is in the paramagnetic phase. This is a clear demonstration that the origin of the voltage at room temperature lies in the spin Seebeck effect. Similar data were obtained at low temperatures for both samples where the AF material is in the spin-folp phase. As discussed earlier, this voltage is due to the charge current in the Pt layer produced by the ISHE conversion of the spin current generated by the temperature gradient across the $RbMnF_3$ slab. In uniaxial AFs, such as MnF_2 and FeF_2, the thermal spin current in the ordered phase is carried by the two magnon modes. Thus, since the thermal magnon populations vanish at $T = 0$, the SSE also vanishes at this temperature. As predicted theoretically [49–51] and confirmed experimentally [18,21] as the temperature increases the SSE increases rapidly with increasing T, reaches a maximum at some T that depends on the material parameters, and then gradually decreases to a minimum at T_N.

Various quantities are used in the literature to quantify the SSE so as to compare the size of the effect in various devices. One of them is the SSE thermopower, defined by [52]

$$TP_{SSE} = \frac{V_{SSE}}{l\,(\Delta T/t)}, \tag{1}$$

where l is the distance between the contacts used to measure the voltage and t is thickness of the device. As pointed out in Ref. [52], the temperature difference ΔT across the $RbMnF_3$ slab is smaller than the temperature difference ΔT_{set} measured by the two thermometers because of the temperature drop in the two varnish layers. Figure 3(b) shows the ratio $\Delta T/\Delta T_{set}$

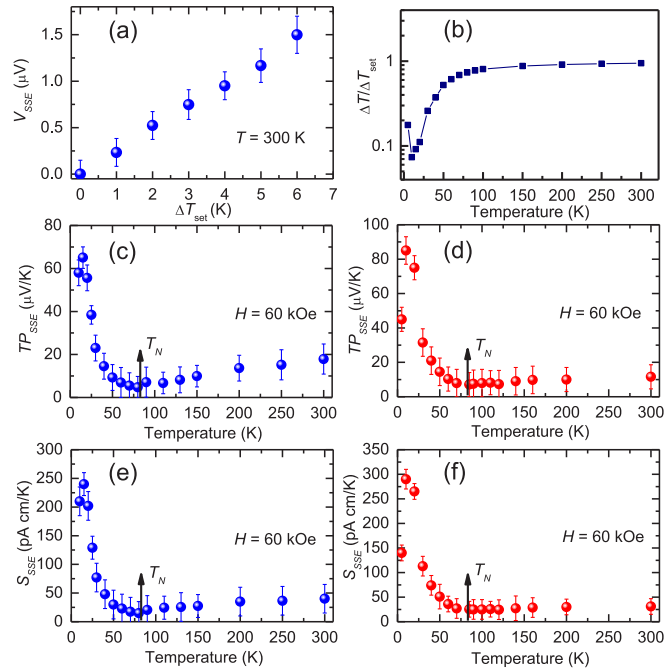

FIG. 3. (a) Variation with applied temperature difference ΔT_{set} of the spin Seebeck voltage V_{SSE} measured in sample B of $RbMnF_3$/Pt for $H = 60\,kOe$ in the paramagnetic phase at $T = 300\,K$. (b) Variation with temperature of the ratio $\Delta T/\Delta T_{set}$ calculated using the data for the thermal conductivities of $RbMnF_3$ and GE varnish. (c) and (d) Temperature dependencies of the spin Seebeck thermopower TP_{SSE} measured in samples B and R with $H = 60\,kOe$. (e) and (f) Temperature dependencies of spin Seebeck coefficient S_{SSE} measured in the two samples with $H = 60\,kOe$.

calculated using the temperature dependence of the thermal conductivity of $RbMnF_3$ reported in Ref. [53] and the data for GE varnish provided by the manufacturer. Surprisingly, even though the thickness of each varnish layer is only 4 μm, compared to 1 mm of the sample slab, the fact that the thermal conductivity of $RbMnF_3$ increases sharply at low temperatures results in the large drop in the ratio $\Delta T/\Delta T_{set}$ shown in Fig. 3(b). Figures 3(c) and 3(d) show the temperature dependencies of TP_{SSE} for the two $RbMnF_3$ samples measured in a field $H = 60$ kOe obtained with the measured voltages and the temperature difference ΔT as in Fig. 3(b). An alternative quantity used to quantify the SSE is the spin Seebeck coefficient as defined in Ref. [51],

$$S_{SSE} = I_{SSE}/|\nabla T| = TP_{SSE}l/R_{Pt}, \quad (2)$$

where R_{Pt} is the Pt strip resistance between the contacts. This has the advantage over the previous quantity because it does not depend on the resistance of the Pt layer that varies with its thickness, width, length, and temperature. Figures 3(e) and 3(f) show the temperature dependencies of S_{SSE} for the two $RbMnF_3$ samples obtained with the measured voltages, the temperature difference ΔT given in Fig. 3(b) and the temperature variation of the resistance of the two Pt strips.

Clearly, in the spin-flop phase, the SSE behaves similarly to uniaxial AFs, it reaches a maximum at some low T and decreases rapidly with increasing T to a minimum at T_N. However, whereas in MnF_2 and FeF_2, the SSE decays substantially as T increases above T_N and becomes negligible at room temperature [18,21], in $RbMnF_3$ the SSE is enhanced in the paramagnetic phase as shown in Figs. 3(c)–3(f). Since there is no long-range AF order above T_N, the large SSE signal at high temperatures cannot be attributed to the spin current carried by AF magnons. It turns out that even in the absence long-range order, in the paramagnetic phase, there is a magnetization under an applied field, which in the case of $RbMnF_3$, is comparable to the one in the ordered phase as shown in Fig. 1(c). This can lead to spin current generation by a thermal gradient mediated by some form of magnetic fluctuations as observed experimentally in paramagnetic insulator/normal metal bilayers [54] and explained theoretically [55,56]. The enhanced SSE in the paramagnetic phase of $RbMnF_3$ reported here is not explained by the existing theories. We attribute this enhancement to a combination of the free spin fluctuations of paramagnetic insulators [56] with the thermal conduction of long-lived paramagnons made possible by the short-range order that persists above T_N [57,58]. A theory for this interesting effect is still lacking.

To summarize, we have presented measurements of the spin Seebeck effect in bilayers made of bulk samples of $RbMnF_3$ with the shape of a slab and thin Pt film strips. The experiments were carried out in two similar samples. By applying a thermal gradient perpendicular to the slab plane, we detect an electric voltage along the Pt strip due to the spin to charge current resulting from the conversion of the thermally generated spin current through the inverse spin Hall effect. By varying the magnetic field applied on the plane of the slab in the range $-80\,\text{kOe} < H < +80\,\text{kOe}$ we observe the antisymmetric step variation typical of the SSE both in the spin-flop and paramagnetic phases. Surprisingly, the SSE increases with temperature and, in the paramagnetic phase above $T_N = 83$ K, the signal is comparable to the values in the ordered phase and increases with T. We attribute this enhanced SSE in the paramagnetic phase to the thermal conduction of long-lived paramagnons made possible by the short-range order that persists above T_N. We hope our results will stimulate the development of additional theories for the spin Seebeck effect mediated by paramagnons in antiferromagnetic materials.

The authors are thankful to J. E. Abrão and E. Gomes for kindly sputtering the platinum strips on the samples and to Dr. D. Ratkovski for the RDX measurement. This research was supported by Conselho Nacional de Desenvolvimento Científico e Tecnológico (CNPq), Coordenação de Aperfeiçoamento de Pessoal de Nível Superior (CAPES), Financiadora de Estudos e Projetos (FINEP), and Fundação de Amparo à Ciência e Tecnologia do Estado de Pernambuco (FACEPE).

[1] K. Uchida, S. Takahashi, K. Harii, J. Ieda, W. Koshibae, K. Ando, S. Maekawa, and E. Saitoh, Observation of spin Seebeck effect, Nature (London) **455**, 778 (2008).

[2] G. E. W. Bauer, E. Saitoh, and B. J. van Wees, Spin caloritonics, Nat. Mater. **11**, 391 (2012).

[3] S. M. Rezende, R. L. Rodríguez-Suárez, R. O. Cunha, A. R. Rodrigues, F. L. A. Machado, G. A. Fonseca Guerra, J. C. Lopez Ortiz, and A. Azevedo, Magnon spin-current theory for the longitudinal spin-Seebeck effect, Phys. Rev. B **89**, 014416 (2014).

[4] S. R. Boona, R. C. Myers, and J. P. Heremans, Spin caloritonics, Energy Environ. Sci. **7**, 885 (2014).

[5] K. Uchida, M. Ishida, T. Kikkawa, A. Kirihara, T. Murakami, and E. Saitoh, Longitudinal spin Seebeck effect: From fundamentals to applications, J. Phys.: Condens. Matter **26**, 343202 (2014).

[6] H. Yu, S. D. Brechet, and J.-P. Ansermet, Spin caloritronics, origin and outlook, Phys. Lett. A **381**, 825 (2017).

[7] K.-I. Uchida, Spin Caloritronics, *Materials Science and Materials Engineering* (Elsevier, Amsterdam, 2022).

[8] S. Maekawa, T. Kikkawa, H. Chudo, J.-I. Ieda, and E. Saitoh, Spin and spin current—From fundamentals to recent progress, J. Appl. Phys. **133**, 020902 (2023).

[9] T. Kikkawa and E. Saitoh, Spin seebeck effect: Sensitive probe for elementary excitation, spin correlation, transport, magnetic order, and domains in solids, Annu. Rev. Condens. Matter Phys. **14**, 129 (2023).

[10] K. Uchida, J. Xiao, H. Adachi, J. Ohe, S. Takahashi, J. Ieda, T. Ota, Y. Kajiwara, H. Umezawa, H. Kawai, G. E. W. Bauer, S. Maekawa, and E. Saitoh, Spin Seebeck insulator, Nat. Mater. **9**, 894 (2010).

[11] J. E. Hirsch, Spin Hall Effect, Phys. Rev. Lett. **83**, 1834 (1999).

[12] A. Azevedo, L. H. Vilela-Leão, R. L. Rodríguez-Suárez, A. B. Oliveira, and S. M. Rezende, dc effect in ferromagnetic resonance: Evidence of the spin-pumping effect? J. Appl. Phys. **97**, 10C715 (2005).

[13] E. Saitoh, M. Ueda, H. Miyajima, and G. Tatara, Conversion of spin current into charge current at room temperature: Inverse spin-Hall effect, Appl. Phys. Lett. **88**, 182509 (2006).

[14] A. Hoffmann, Spin hall effects in metals, IEEE Trans. Magn. **49**, 5172 (2013).

[15] J. Sinova, S. O. Valenzuela, J. Wunderlich, C. H. Back, and T. Jungwirth, Spin hall effects, Rev. Mod. Phys. **87**, 1213 (2015).

[16] K. Uchida, H. Adachi, T. Ota, H. Nakayama, S. Maekawa, and E. Saitoh, Observation of longitudinal spin-Seebeck effect in magnetic insulators, Appl. Phys. Lett. **97**, 172505 (2010).

[17] S. Seki, T. Ideue, M. Kubota, Y. Kozuka, R. Takagi, M. Nakamura, Y. Kaneko, M. Kawasaki, and Y. Tokura, Thermal Generation of Spin Current in an Antiferromagnet, Phys. Rev. Lett. **115**, 266601 (2015).

[18] S. M. Wu, W. Zhang, Amit KC, P. Borisov, J. E. Pearson, J. S. Jiang, D. Lederman, A. Hoffmann, and A. Bhattacharya, Antiferromagnetic Spin Seebeck Effect, Phys. Rev. Lett. **116**, 097204 (2016).

[19] J. Holanda, D. S. Maior, O. Alves Santos, L. H. Vilela-Leão, J. B. S. Mendes, A. Azevedo, R. L. Rodríguez-Suárez, and S. M. Rezende, Spin Seebeck effect in the antiferromagnet nickel oxide at room temperature, Appl. Phys. Lett. **111**, 172405 (2017).

[20] Y. Shiomi, R. Takashima, D. Okuyama, G. Gitgeatpong, P. Piyawongwatthana, K. Matan, T. J. Sato, and E. Saitoh, Spin Seebeck effect in the polar antiferromagnet $\alpha - Cu_2V_2O_7$, Phys. Rev. B **96**, 180414(R) (2017).

[21] J. Li, Z. Shi, V. H. Ortiz, M. Aldosary, C. Chen, V. Aji, P. Wei, and J. Shi, Spin Seebeck Effect from Antiferromagnetic Magnons and Critical Spin Fluctuations in Epitaxial FeF_2 Films, Phys. Rev. Lett. **122**, 217204 (2019).

[22] P. R. T. Ribeiro, F. L. A. Machado, M. Gamino, A. Azevedo, and S. M. Rezende, Spin Seebeck effect in antiferromagnet nickel oxide in wide ranges of temperature and magnetic field, Phys. Rev. B **99**, 094432 (2019).

[23] W. Yuan, J. Li, and J. Shi, Spin current generation and detection in uniaxial antiferromagnetic insulators, Appl. Phys. Lett. **117**, 100501 (2020).

[24] A. H. MacDonald and M. Tsoi, Antiferromagnetic metal spintronics, Philos. Trans. R. Soc., A **369**, 3098 (2011).

[25] V. M. T. S. Barthem, C. V. Colin, H. Mayaffre, M.-H. Julien, and D. Givord, Revealing the properties of Mn_2Au for antiferromagnetic spintronics, Nat. Commun. **4**, 2892 (2013).

[26] E. V. Gomonay and V. M. Loktev, Spintronics of antiferromagnetic systems, Low Temp. Phys. **40**, 17 (2014).

[27] T. Jungwirth, X. Marti, P. Wadley, and J. Wunderlich, Antiferromagnetic spintronics, Nat. Nanotechnol. **11**, 231 (2016).

[28] J. B. S. Mendes, R. O. Cunha, O. Alves Santos, P. R. T. Ribeiro, F. L. A. Machado, R. L. Rodriguez-Suarez, A. Azevedo, and S. M. Rezende, Large inverse spin Hall effect in the antiferromagnetic metal Ir20Mn80, Phys. Rev. B **89**, 140406(R) (2014).

[29] W. Zhang, M. B. Jungfleisch, W. Jiang, J. E. Pearson, A. Hoffmann, F. Freimuth, and Y. Mokrousov, Spin Hall Effects in Metallic Antiferromagnets, Phys. Rev. Lett. **113**, 196602 (2014).

[30] O. Gomonay, T. Jungwirth, and J. Sinova, Concepts of antiferromagnetic spintronics, Phys. Status Solidi RRR **11**, 1700022 (2017).

[31] M. B. Jungfleisch, W. Zhang, and A. Hoffmann, Perpectives of antiferromagnetic spintronics, Phys. Lett. A **382**, 865 (2018).

[32] V. Baltz, A. Manchon, M. Tsoi, T. Moriyama, T. Ono, and Y. Tserkovnyak, Antiferromagnetic spintronics, Rev. Mod. Phys. **90**, 015005 (2018).

[33] T. Jungwirth, J. Sinova, A. Manchon, X. Marti, J. Wunderlich, and C. Felser, The multiple directions of antiferromagnetic spintronics, Nat. Phys. **14**, 200 (2018).

[34] S. S. P. Parkin *et al.*, Exchange-biased magnetic tunnel junctions and application to nonvolatile magnetic random access memory, J. Appl. Phys. **85**, 5828 (1999).

[35] J. Nogués and I. K. Schuller, Exchange bias, J. Magn. Magn. Mater. **192**, 203 (1999).

[36] J. R. Fermin, M. A. Lucena, A. Azevedo, F. M. de Aguiar, and S. M. Rezende, Measurements of exchange anisotropy in NiFe/NiO films with different techniques, J. Appl. Phys. **87**, 6421 (2000).

[37] F. Keffer, Anisotropy in the Antiferromagnetic MnF_2, Phys. Rev. **87**, 608 (1952).

[38] J. Barak, V. Jaccarino, and S. M. Rezende, The magnetic anisotropy of MnF_2, at 0 K, J. Magn. Magn. Mater. **9**, 323 (1978).

[39] D. T. Teaney, M. J. Freiser, and R. W. H. Stevenson, Discovery of a Simple Cubic Antiferromagnet: Antiferromagnetic Resonance in $RbMnF_3$, Phys. Rev. Lett. **9**, 212 (1962).

[40] P. H. Cole and W. J. Ince, Equilibrium spin configuration and resonance behavior of $RbMnF_3$, Phys. Rev. **150**, 377 (1966).

[41] W. J. Ince, Coupled antiferromagnetic-nuclear-magnetic resonance in $RbMnF_3$, Phys. Rev. **184**, 574 (1969).

[42] A. Kornblit and G. Ahlers, Heat capacity of $RbMnF_3$ near the antiferromagnetic transition temperature, Phys. Rev. B **8**, 5163 (1973).

[43] E. E. Bragg and M. S. Seehra, Magnetic susceptibity of $RbMnF_3$, Phys. Lett. A **39**, 29 (1972).

[44] L. J. de Jongh and D. J. Breed, Antiferromagnetic susceptibity of $RbMnF_3$. Evidence for a temperature dependence of the exchange constant, Solid State Commun. **15**, 1061 (1974).

[45] Y. Shapira and N. F. Oliveira, Jr., Crossover behavior of the magnetic phase boundary of the isotropic antiferromagnet $RbMnF_3$ from ultrasonic measurements, Phys. Rev. B **17**, 4432 (1978).

[46] U. Köbler and A. Hoser, Single domain behaviour of bulk $RbMnF_3$, J. Magn. Magn. Mater. **325**, 87 (2013).

[47] J. C. López Ortiz, G. A. Fonseca Guerra, F. L. A. Machado, and S. M. Rezende, Magnetic anisotropy of antiferromagnetic $RbMnF_3$, Phys. Rev. B **90**, 054402 (2014).

[48] C. T. Bui and F. Rivadulla, Anomalous and Planar Nernst effects in thin-films of half-metallic ferromagnet $La_{2/3}Sr_{1/3}MnO_3$, Phys. Rev. B **90**, 100403(R) (2014).

[49] Y. Ohnuma, H. Adachi, E. Saitoh, and S. Maekawa, Spin Seebeck effect in antiferromagnets and compensated ferrimagnets, Phys. Rev. B **87**, 014423 (2013).

[50] S. M. Rezende, R. L. Rodríguez- Suárez, and A. Azevedo, Theory of the spin Seebeck effect in antiferromagnets, Phys. Rev. B **93**, 014425 (2016).

[51] S. M. Rezende, R. L. Rodríguez-Suárez, and A. Azevedo, Magnon diffusion theory for the spin Seebeck effect in ferromagnetic and antiferromagnetic insulators, J. Phys. D: Appl. Phys. **51**, 174004 (2018).

[52] R. Iguchi, K.-I. Uchida, S. Daimon, and E. Saitoh, Concomitant enhancement of the longitudinal spin Seebeck effect and the

thermal conductivity in a Pt/YIG/Pt system at low temperatures, Phys. Rev. B **95**, 174401 (2017).

[53] J. Gustafson and C. T. Walker, Thermal conductivity in two simple antiferromagnets, $RbMnF_3$ and MnF_2, Phys. Rev. B **8**, 3309 (1973).

[54] S. M. Wu, J. E. Pearson, and A. Bhattacharya, Paramagnetic Spin Seebeck Effect, Phys. Rev. Lett. **114**, 186602 (2015).

[55] Y. Yamamoto, M. Ichioka, and H. Adachi, Antiferromagnetic spin Seebeck effect across the spin-flop transition: A stochastic Ginzburg-Landau simulation, Phys. Rev. B **105**, 104417 (2022).

[56] K. Oyanagi, S. Takahashi, T. Kikkawa, and E. Saitoh, Mechanism of paramagnetic spin Seebeck effect, Phys. Rev. B **107**, 014423 (2023).

[57] M. Fidrysiak and J. Spałek, Stable high-temperature paramagnons in a three-dimensional antiferromagnet near quantum criticality: Application to $TlCuCl_3$, Phys. Rev. B **95**, 174437 (2017).

[58] Y. Zheng, T. Lu, Md M. H. Polash, M. Rasoulianboroujeni, N. Liu, M. E. Manley, Y. Deng, P. J. Sun, X. L. Chen, R. P. Hermann, D. Vashaee, J. P. Heremans, and H. Zhao, Paramagnon drag in high thermoelectric figure of merit Li-doped MnTe, Sci. Adv. **5**, eaat9461 (2019).